Contents lists available at ScienceDirect

Applied Catalysis B: Environmental

Letter to the Editor

Building of anti-restack 3D BiOCl hierarchitecture by ultrathin nanosheets towards enhanced photocatalytic activity

A R T I C L E   I N F O

A B S T R A C T

A characteristic anti-restack 3D BiOCl hierarchitecture constructed by ultrathin BiOCl nanosheets assembled substructures has been designed and synthesized via a facile hydrothermal route. The graphene-like ultrathin BiOCl nanosheets with thickness of about 3.7 nm expose the renowned energetically active (0 0 1) facet, enabling the fast separation and transport of photogenerated electron–hole pairs. Meanwhile, the multi-reflection of light and large surface area of the formed 3D nano-velvet substructures enhance the light harvest and molecule adsorption capability. Consequently, the resultants show a superior photocatalytic performance of 99% photodegradation and corresponding 74% mineralization for rhodamine B within 10 min, and an outstanding photocurrent response under solar light illumination. What is more, the unique microstructure efficiently overcomes the restack of ultrathin nanosheets. This work develops a feasible strategy that utilizes ultrathin nanosheets to design and synthesize anti-restack hierarchitectures for establishing efficacious photocatalytic and water splitting systems.

© 2015 Elsevier B.V. All rights reserved.

1. Introduction

Morphology engineering is an effective strategy to enable semiconductor photocatalysts with an excellent solar light photocatalytic performance [1–3]. Therefore, over years, photocatalysts with various morphologies have been substantially developed and applied for environmental remediation [4–7]. Particularly, ultrathin nanosheet semiconductor photocatalysts have triggered a high research enthusiasm in recent years, because of their superior photoactivity that originates from the advantage of promoting separation/transport of charge carriers and large surface area of ultrathin nanosheet [8–13]. However, an encountered challenge when using ultrathin nanosheets is the tendency to restack during processing, which persecutes and restricts their storage and longterm applications. From this point of view, it is promising to design three-dimensional (3D) hierarchical architecture constructed by these ultrathin nanosheets to minimize the corresponding possibility of agglomeration.

Benefiting from the typical layered structure featured as $[Bi_2O_2]^{2+}$ layers being sandwiched between two slabs of chloride ions, bismuth oxychloride (BiOCl) exhibits a comparable or even better photocatalytic performance than that of anatase TiO_2 [14]. The polarized valence band resulted from the hybridization of Bi6s and O2p orbits generates a self-induced internal electric field perpendicular to the (0 0 1) plane, facilitating separation of photo-generated electron–hole pairs along the [0 0 1] direction [15–17]. Moreover, it is easy to attain activated oxygen molecule through one-electron transfer on (0 0 1) surface and the resultant oxygen radicals are of great advantages to mineralize the dyes in the solution [18]. In addition, the strong intra-layer

bonding and the weak interlayer Van der Waals interactions are conducive to the exfoliation of bulk BiOCl to form ultra-thin sheets, which could reduce the recombination rate of the photogenerated charges by shortening the diffusion length [9,16–20]. Micro-assembly of BiOCl nanosheets has been proven to be a feasible strategy to improve the photocatalytic activity and recycling character [21–25]. However, the thickness of the previous reported BiOCl nanosheets is almost limited to several tens of nanometers. Chen's group reported the ultrathin nanosheets assembled porous micriflowers BiOCl with superior photosensitized degradation [25]. But the photodegradation efficiency has obviously decreased during the cycling experiment. Thus, it is indispensable to assemble the ultrathin nanosheets BiOCl into specially designed 3D micro/nanostructures achieving high-activity and high-stability for practical application

For this purpose, herein, the unique 3D BiOCl (UBOC) hierarchitecture, in which ultrathin nanosheets assembled nano-velvet substructures are formed on the surface of micro-scaffold, is synthesized. The ultrathin nanosheet with active (0 0 1) plane as the main surface is about five atomic-layers in thickness, allowing the facilitative separation and transport of photogenerated charge carries. Such 3D microstructure presents an excellent photocatalytic performance: 99% decolouration and 74 % removal of total organic carbon (TOC) for rhodamine B (RhB) were achieved within 10 min under AM1.5 solar light irradiation. According to the merit of antirestack and easy recyclability of the hierarchitecture, we believe that this work broadens the possibility of designing efficient photocatalyst using ultrathin nanosheets. The pronounced photocurrent of the photoelectrode also qualifies the structure as a potential candidate in water splitting.
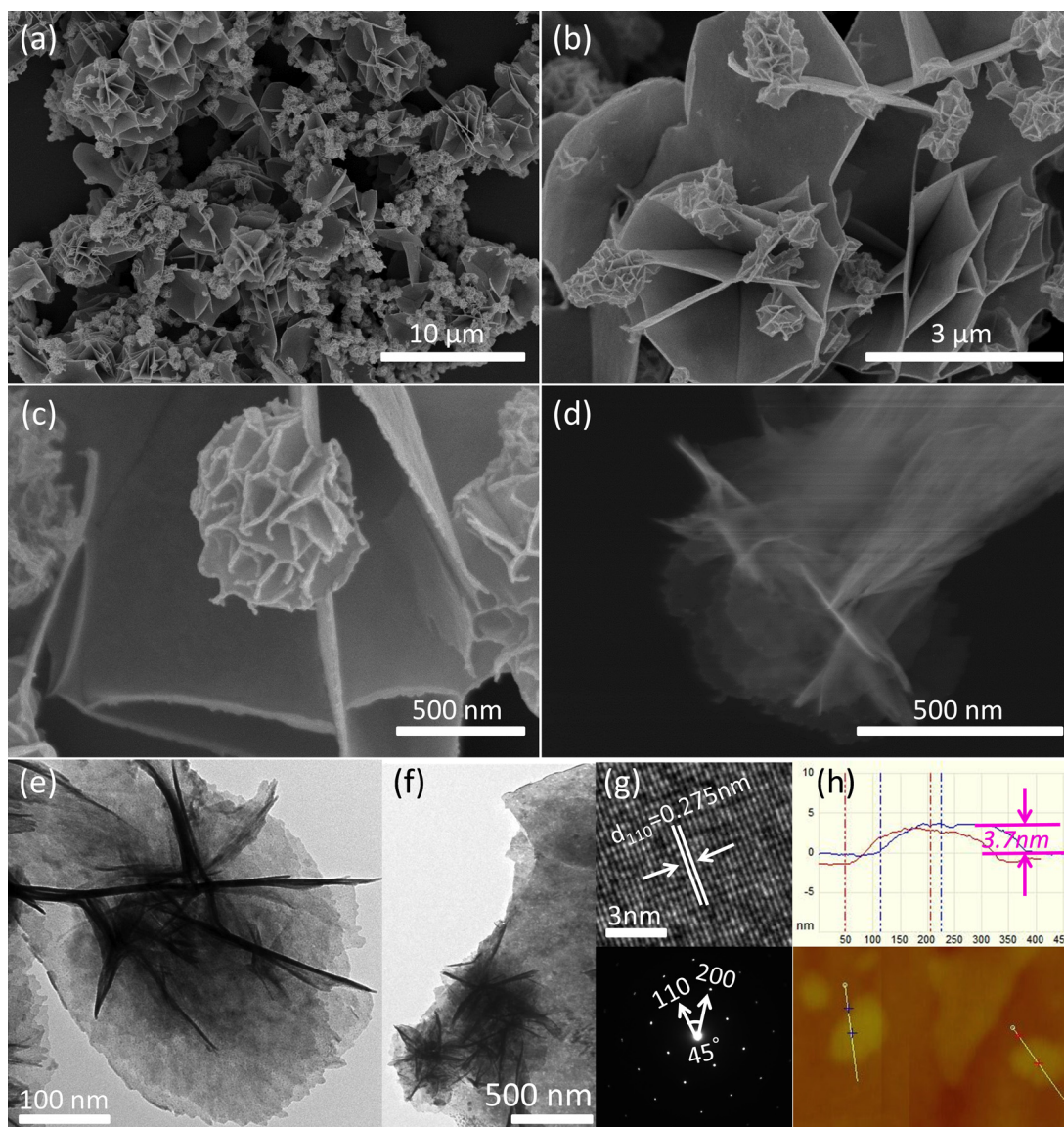
Fig. 1. (a–d) SEM images; (e–f) TEM images; (g) top: HRTEM, and bottom: SAED pattern, and (h) AFM image and the corresponding height profile of UBOC.

2. Experimental details

2.1. Materials

All the chemicals were of analytic grade purity, got from Sigma-Aldrich Co. LLC, and used as received without further purification.

2.2. Synthesis of the UBOC

The novel 3D BiOCl hierarchical architectures were synthesized using a surfactant assisted hydrothermal process. In a typical synthesis, 0.485 g of $Bi(NO_3)_3$ $5H_2O$ was dissolved in 20 mL of 0.1 M HNO_3 solution with vigorous stirring for 20 min to get a transparent solution. Next, 0.01 g octylphenol polyoxyethylene ether (10) (OP-10) surfactant was added into the above transparent solution. Then, 0.149 g of KCl was added into the solution with vigorous stirring, yielding a uniform white suspension. After another 30 min of agitation, the mixture was transferred into a 25 mL capacity Teflon-lined stainless steel autoclave, and this autoclave was kept at 120 °C for 6 h and then cooled to room temperature naturally. The resulting white solid powder was collected by centrifugation and washed

with deionized water several times to remove residual ions. The final products were then dried at 30 °C for 24 h for further characterization. In addition, the product obtained without the addition of OP-10 surfactant under the same condition was prepared as a comparison.

2.3. Characterizations

Powder X-ray diffraction pattern (XRD) was recorded on Bruker D8 Advance equipped with graphite monochromatized high-intensity Cu Kα radiation ($\lambda = 1.54178$ Å). The scanning electron microscopy (SEM) images were obtained by HITACHI S4800 scanning electron microscope. The transmission electron microscopy (TEM) images were obtained by JEOL JEM-2010F operated at an acceleration voltage of 100 kV. High-resolution transmission electron microscopy (HRTEM) image and the corresponding selected area electron diffraction (SAED) analyses were attained at an acceleration voltage of 200 kV. X-ray photoemission spectroscopy (XPS) was recorded on a VG MultiLab 2000 system with a monochromatic Al Kα source operated at 300 W. Tapping-mode atomic force microscopy (AFM) image was obtained on DI Innova

Multimode SPM platform. Room-temperature UV–vis absorption spectroscopy and diffuse reflectance spectroscopy were carried out on Varian Cary 5000 UV–vis-NIR spectrophotometer. The Brunauer–Emmett–Teller (BET) surface areas were measured by nitrogen adsorption on ASAP2020 M accelerated surface area and porosimetry system.

2.4. Photocatalytic activity measurements

Solar light photocatalytic activities of the synthesized products were evaluated by examining the photodegradation of RhB under AM 1.5 solar light irradiation (Newport solar simulator with 300 W Xe lamp). Typically, 10 mg of synthesized products were added into 50 mL of 2.0×10^{-5} M RhB or NBT (Nitro blue tetrazolium chloride) aqueous solution. Before illumination, the suspension was placed in the dark under constant stirring for 90 min to reach adsorption/desorption equilibrium. Five milliliters of the suspension were taken out every 5 min (every 10 min for NBT), and centrifuged to remove the photocatalysts for UV–vis absorption spectrum measurements. The concentration of RhB and NBT were determined by monitoring the characteristic absorption peak at 554 nm and 260 nm, respectively. To measure the mineralization rate, a TOC-VCPH analyser was used to analyse the TOC of the degraded dyes.

2.5. Photoelectrochemical measurements

The indium doped tin oxide (ITO, PGO Glass CEC020P, Germany) substrates were cleaned by ultrasonication in deionized water, absolute ethanol, and isopropanol for 15 min sequentially. All the edges of ITO glass substrates were covered by AB glue. Typically, the aqueous slurries of the surfactant assisted BiOCl samples were spread on ITO glass substrates. The suspension was prepared by grinding 20 mg of the BiOCl samples, 40 μL of PEDOT-PSS (Sigma–Aldrich, 1.3–1.7%) aqueous solution and 200 μL of deionized water (DI) water. The spread films were dried in air and annealed at 150 °C for 10 min. The photocurrents were measured by an electrochemical analyser (BioLogic SP-200) in a standard three-electrode system with the BiOCl films as the working electrodes, a Pt mesh as the counter electrode, and Ag/AgCl as a reference electrode. All three electrodes were placed in a glass cell with a 2 in.^{2} quartz window. A simulated AM 1.5 illumination served as light source and 0.5 M Na_2SO_4 aqueous solution was used as the electrolyte which was bubbled by N_2 thoroughly to remove the dissolved oxygen before the measurement.

3. Results and discussion

As shown in Fig. 1a–b, unlike conventional BiOCl hierarchical architectures, the prepared sample presents a characteristic flower-like morphology. Large quantities of nano-sized velvet flowers are formed on the surface of scaffold which constructed by microplates. The microplates have the width of 1–3 μm and thickness of 20–40 nm. The nano velvet flowers are organized by ultrathin nanosheets with width of around 400 nm and thickness of less than 10 nm. Such unique structure could be dispersed in the solution as a high-efficient catalyst without concerning the aggregation of the particles.

The velvet-flower substructures were further characterized by TEM and HRTEM. As presented in Fig. 1e–f, the velvet flowers are assembled by ultrathin nanosheets with size of around 200 nm, and thickness of around 5 nm. Lattice fringes with a lattice spacing of 0.275 nm corresponding to that of the (1 1 0) facets for nanosheets are clearly shown in Fig. 1g (top). And the corresponding selected area electron diffraction (SAED) pattern (Fig. 1g (bottom)) exhibits a regular and clear square diffraction spot array, demonstrating that

the as-prepared products are of high crystalline quality. Considering that the angle between the (0 0 1) and (1 1 0) facets is 90°, the exposed surface of the nanosheet belongs to (0 0 1) facets. This feature enables the product with a higher photocatalytic capability than the samples with other facets, owing to the existence of the polarized self-induced internal electric field perpendicular to the ultra-thin (0 0 1) facets [15] and the preferential formation of $^\bullet O_2 -$ through only one electron transfer over (0 0 1) facet when the sample is soaked in O_2 dissolved aqueous solution [18]. Furthermore, more reliable information on the thickness and size of the ultra-thin nanosheets was obtained from the AFM measurement (shown in Fig. 1h). The thickness of the ultrathin nanosheets is estimated to be ∼3.7 nm, and the size is consistent with that measured from the TEM images. As demonstrated in Fig. S1a, without the addition of OP-10 surfactant, the velvet-flower substructures do not show up, indicating that OP-10 is the key factor for growing the UBOC. In this condition, the product is nominated as conventional 3D BiOCl microstructure (CBOC).

XPS was conducted in order to investigate the surface compositions and chemical states of UBOC (Fig. S2). The peak at 284.5 eV could be readily assigned to the binding energies of C 1s, attributed to the adventitious carbon on the surface of the sample that is nearly unavoidable. Two strong peaks at 158 eV and 164 eV separately result from Bi $4f_{7/2}$ and Bi $4f_{5/2}$, corresponding to Bi^{3+} [26]. In combination with binding energy peak at 197 eV relevant to Cl $2p_{3/2}$ and the sharp peak at 530 eV that stems from bismuth-oxygen bond, it is concluded that the as-synthesized product is BiOCl. And the XPS data presented in Fig. S2 further verify the composition of BiOCl.

It is of great interest to propose the formation mechanism of the UBOC. As demonstrated, BiOCl is preferable to form microplates and microplates assembled 3D hierarchitectures [21–24,27–28]. During our experiment, the non-ionic surfactant OP-10 molecules were adsorbed via the possibility of hydrogen bonding between ethoxyl oxygen atoms with terminated oxygen atoms on the BiOCl surface. The high concentration of adsorbed OP-10 molecules on the high density of terminated surface oxygen atoms (0 0 1) facet hinders the formation of BiOCl nanosheet along [0 0 1] direction. With the low concentration of surfactant, only partial BiOCl particles grew to ultrathin nanosheets, others were preferred to form microplates. Meanwhile, the high energetic side-surfaces without surfactant adsorbed were tending to aggregate with nanosheets and/or microplates to 3D hierarchitectures.

For better understanding the properties of different morphologies of BiOCl, XRD analysis was applied. In Fig. 2a, all the sharp diffraction peaks in the XRD patterns are perfectly indexed as the tetragonal phase BiOCl with the lattice parameters of $a = 0.3891$ nm and $c = 0.7369$ nm (JCPDS card No. 06-0249), and no peaks from other phases or materials are detected. For UBOC, the diffraction peak ratio of (0 0 1) over (1 1 0) possesses larger value in comparison with that of CBOC, indicative of that UBOC is preferential to grow along the [0 0 1] orientation (c axis) with (0 0 1) facets as the main surface, which is consistent with the HRTEM analysis.

The optical properties of prepared BiOCl samples were characterized by UV/vis absorption spectra (Fig. 2b). It seems like that the band gap of UBOC is similar to CBOC. But actually, the UBOC has slightly smaller band gap and higher visible-light absorption intensity than CBOC, rendering it as a promising photocatalytic material for efficient light harvesting.

The BET specific surface area is one of the main characteristic parameters for photocatalyst. The BET specific surface areas of the relevant samples were evaluated by nitrogen adsorption and desorption measurements, as shown in Fig. 2c. The surface area values calculated from N_2 isotherms at 77 K for UBOC and CBOC are 17.04 $m^2 g^{-1}$ and 9.79 $m^2 g^{-1}$, respectively. Obviously, UBOC possesses larger surface-to-volume ratio, enabling it with
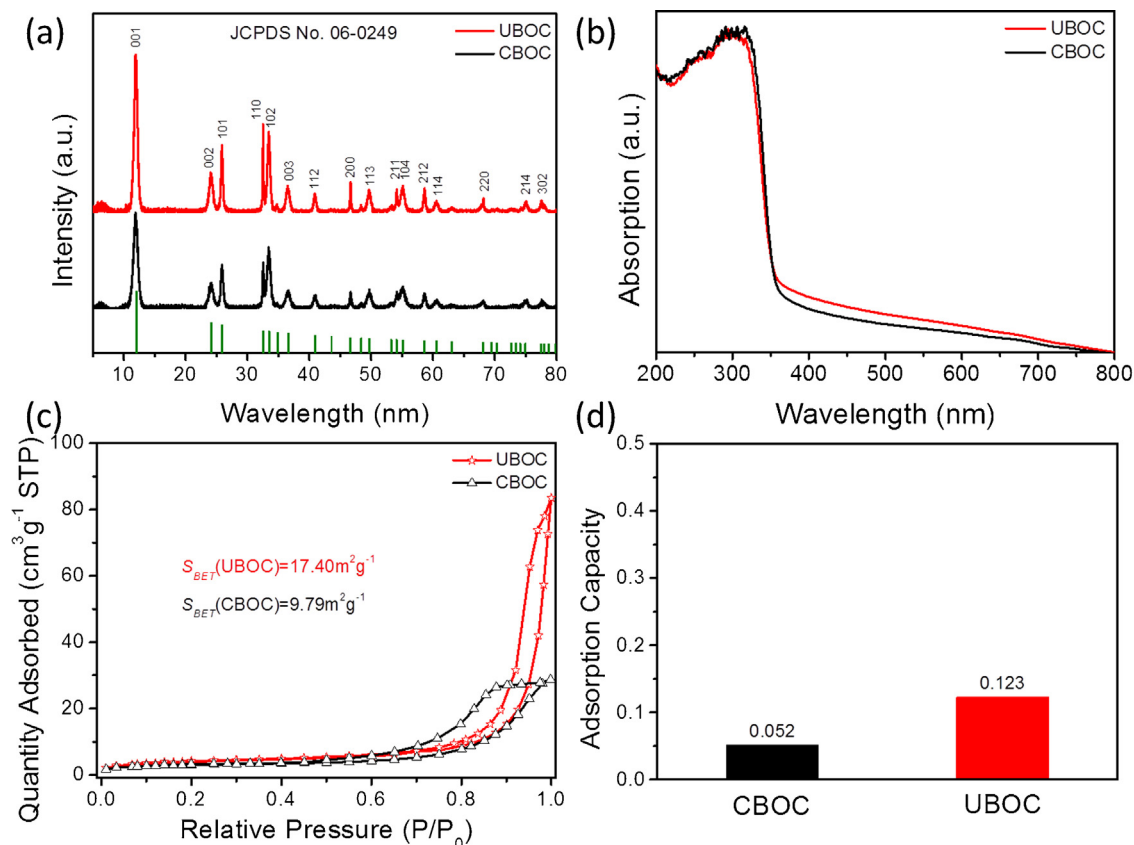
Fig. 2. (a) XRD spectra; (b) UV–vis absorption spectra; (c) nitrogen adsorption–desorption isotherm and (d) time profiles of adsorption RhB in the dark of the samples.

more reaction points for light harvest and molecule adsorption (Fig. 2d). And the exposure of active (0 0 1) facet that has a suitable self-polarized internal electric field favours the separation of photogenerated electron–hole pairs related to the other facets [15–17]. Moreover, considering the c parameter of BiOCl is 0.7369 nm, each nanosheet consists of around 5 [Cl-Bi-O-Bi-Cl] units, efficiently shortening the transport route of charge carriers. Thus, such ultrathin nanosheets constructed velvet-flower nanostructures of UBOC are of high advantages in photocatalytic applications.

All the above analyses point to the fact that UBOC should be a good photocatalyst. The photocatalytic degradation of toxic pollutants or organic dyes represents a general approach to estimate the performance of photocatalysts. The investigation was performed under solar light irradiation with RhB as a probe molecule in aqueous solution. And the corresponding activity of the CBOC is likewise presented for comparison. As characterized, the time profiles for the photodegradation reactions are refined and presented in Fig. 3a. The photodegradation of RhB is negligible in the absence of catalyst under solar light irradiation. The discoloration of RhB in the presence of UBOC and CBOC in the dark is also ignorable. However, the photodegradation reactions with photocatalysts are noticeable under solar light illumination. As shown in Fig. 3a, for 10 min solar light illumination, the photodegradation percentages of RhB are 99% and 52% for UBOC and CBOC, respectively. Moreover, the changes in the TOC reflect the degree of mineralization of an organic molecule during testing period. After solar light irradiation for 10 min, the mineralization efficiencies of UBOC and CBOC are evaluated to be 73.82 % and 29.92 %, separately. Prolonged the irradiation time to 30 min, the mineralization efficiencies are calculated to be 89.96 % and 49.11 %, respectively (Fig. 3b). In addition, the photodegradation percentages of colorless NBT over samples were provided. As depicted in Fig. S3, without the photosensitization

of RhB dye, the decomposition percentages of NBT over UBOC are larger than that of CBOC, demonstrating that ultrathin nanosheets built hierarchical architecture has a better photocatalytic capability than CBOC. The mineralization ratio is not in full accord with the photodegradation ratio, which means the formation of intermediates during the photodegradation process.

The reaction rate of photocatalytic degradation was ultilized to distinguish the photocatalytic performance of UBOC and CBOC. The degradation of dyes could be described by a pseudo-first-order reaction with a simplified Langmuir–Hinshelwood model, $\ln(C_0/C) = kt$, where k is the pseudo-first-order rate constant, C_0 is the initial concentration of RhB and C is the concentration of RhB at different reaction time [16]. As shown in the inset of Fig. 3a, the plots of $\ln(C_0/C)$ versus irradiation time are found to be linear. The corresponding k for the photodegradation of RhB over UBOC and CBOC are fitted to be $0.3004\,min^{-1}$ and $0.0903\,min^{-1}$, respectively (Fig. 3c). To be excited, the k value of UBOC is more than 3 times higher than that of CBOC. In order to more precisely describe the photocatalytic performance, we normalized the reaction rate by the surface area calculated from BET measurement. As illustrated in Fig. 3c, the degradation constant of UBOC ($k' = 0.0173\,g\,min^{-1}\,m^{-2}$) is more than 2 times higher than that of CBOC ($k' = 0.0092\,g\,min^{-1}\,m^{-2}$). Such evidence indicates a superior photocatalytic performance of UBOC that is associated with structural features rather than with the enlarged surface area solely.

In addition, in our work, the reusability and the stability of UBOC are also of high superiority. The photodegradation performance of UBOC does not deteriorate even after being used more than five cycles (Figs. 3d and S3b). Prospectively, the ultrathin nanosheets organized velvet flowers still keep intact after drying and recycling for five times (Fig. S5), showing a good anti-restack property and thus a great potential for industrial applications.
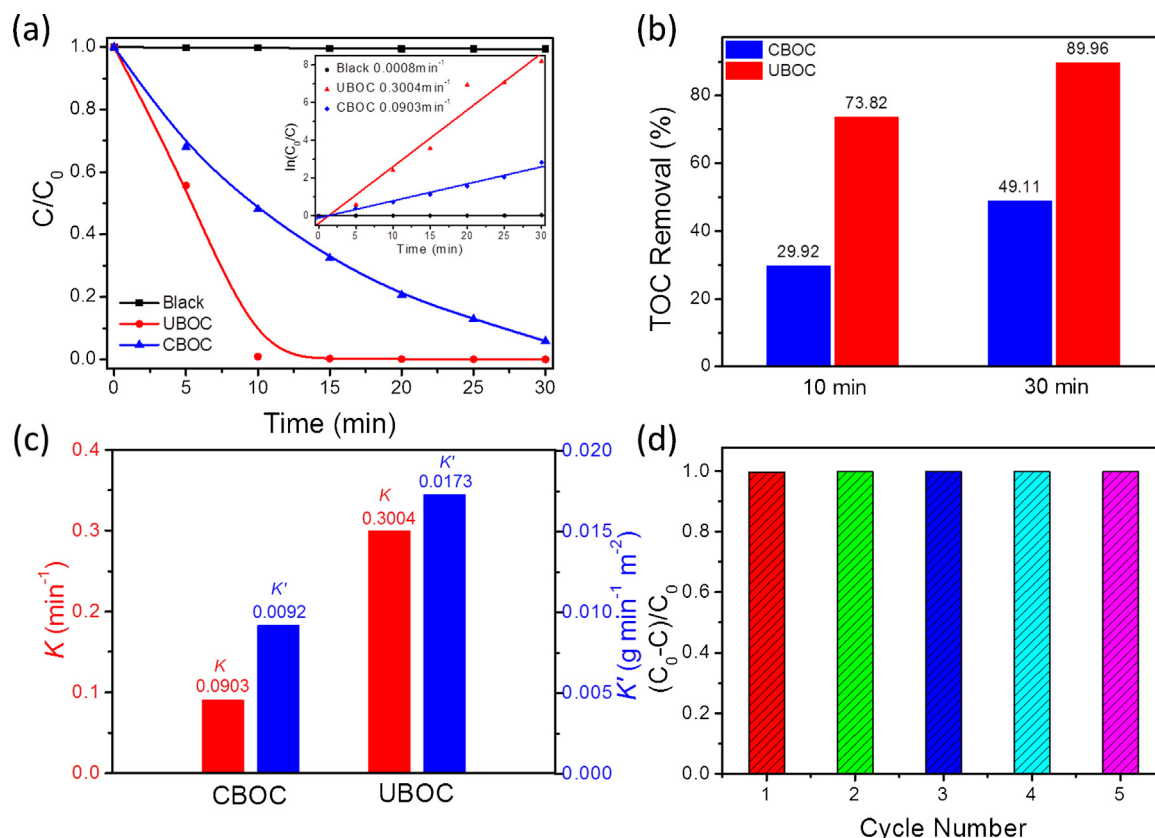
Fig. 3. (a) Time profiles of the photocatalytic degradation of RhB over the samples under solar irradiation; (b) TOC removal of RhB over the samples under solar irradiation for 10–30 min; (c) comparison on the reaction rate constants for photocatalytic degradation of RhB over the samples; and (d) cycles photodegradation efficiency of RhB over UBOC.

Photocatalytic activity is based on the separation and transfer efficiency of the photoinduced charge carriers. The transient photocurrent responses were investigated to determine the photogenerated charge separation efficiency of UBOC and CBOC. The electrochemical measurements were carried out in a typical three-electrode cell. As shown in Fig. 4a and S3, the transient photocurrent responses of UBOC film electrode exhibit a higher photocurrent than that of CBOC electrode, indicating a more efficient interfacial photoinduced charge separation and transfer over UBOC electrode, and a promising application of UBOC in water splitting.

As presented in UV/vis absorption spectra (Fig. 2b), both of the UBOC and CBOC have visible light absorption. The UBOC shows slightly smaller absorption band-gap and stronger visible light absorption intensity than CBOC. The energy of the visible light is too low to induce the intrinsic absorption of wide band-gap BiOCl. However, it is well-known that the surface atoms of BiOCl can escape from the lattice to form relevant vacancy. And the formed vacancies should strongly affect the band structure of semiconductors, which may result in the visible light absorption. With the reducing of thickness, the buried internal atoms could also
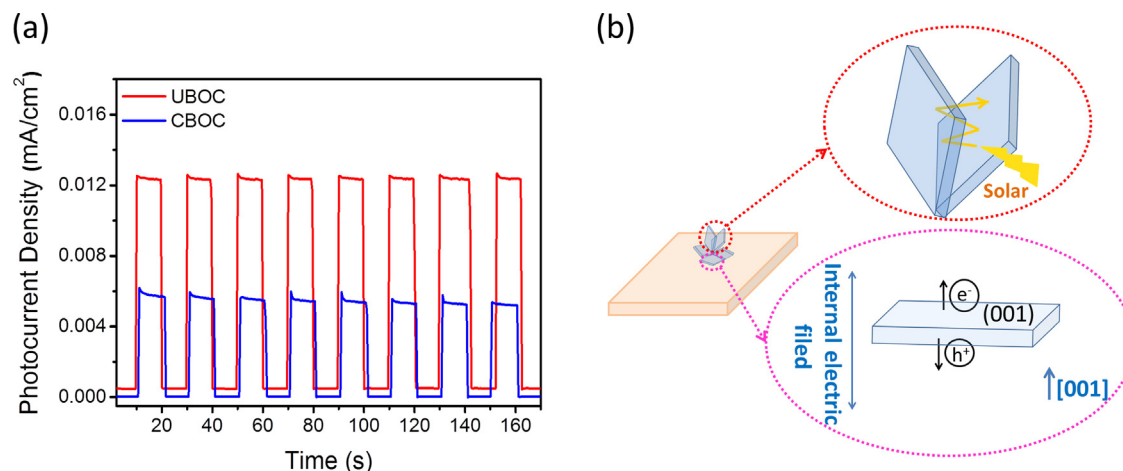
Fig. 4. (a) Transient photocurrent responses at 0.6 V versus Ag/AgCl electrode in 0.5 M Na$_2$SO$_4$ aqueous solution at simulated AM 1.5 illumination; and (b) the schematic of multi-light absorption and photogenerated electron–hole pairs separation/transfer with the help of appropriate internal electric field of BiOCl.
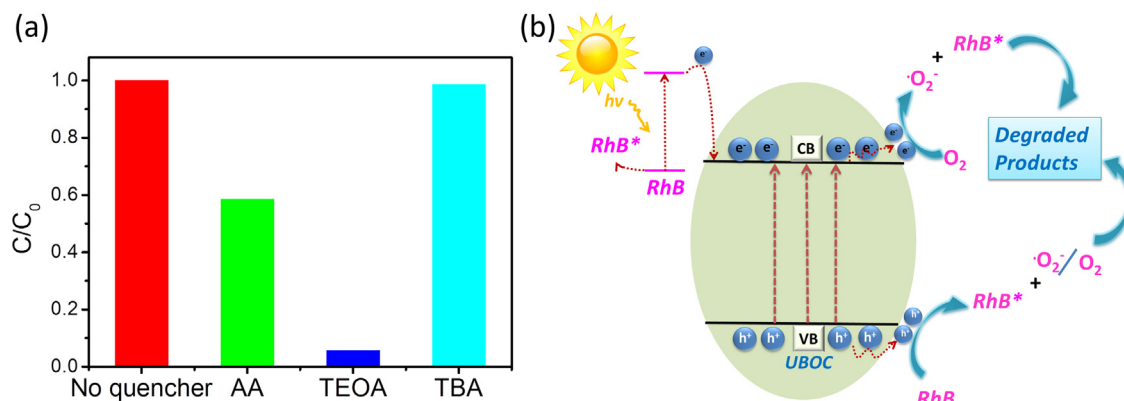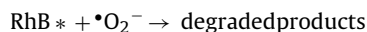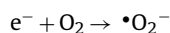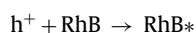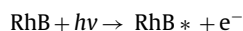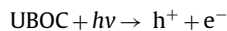
Fig. 5. (a) Photodegradation of RhB over UBOC in the presence of scavengers under solar light irradiation. (b) The schematic diagram illustrating the tentative photodegradation process under solar light irradiation over UBOC.

escape to form vacancy [9]. Thus, comparing with the CBOC, ultrathin nanosheets composed UBOC has more opportunities to form vacancies to enhance the visible light absorption. In addition, the multi-reflection of light among the ultrathin nanosheets in 3D velvet flowers would further enhance the visible-light absorption [29–30] (Fig. 4b up). The enhanced light absorption capability of UBOC could result in more photoinduced electrons and holes. Meanwhile, the layered structure of BiOCl would induce an internal static electric field perpendicular to the (0 0 1) facet [14,31], promoting the effective separation of the photogenerated electro-hole pairs along the [0 0 1] direction by providing an additional driving force (Fig. 4b bottom). Additionally, the five-atomic-layer thickness of ultrathin nanosheets greatly shortens the transport length of the carriers before participating in the photocatalytic reactions, beneficial for reducing the useless recombination.

When the UBOC is irradiated by solar light, electrons could be excited from the valence band to the conduction band, leaving the corresponding holes in the valence band. Meanwhile, the conduction band position of BiOCl is much more positive than the LUMO of RhB [32], facilitating the electrons in the RhB molecules to inject into the conduct band of UBOC. As descripted in literature, the electrons are preferential to form superoxide radicals ($\bullet O_2^-$) through only one electron rather than $\bullet O^{2-}$ through two electrons over BiOCl (0 0 1) facet [18]. Thus, the electrons may reduce the dissolved oxygen molecules to strong oxidative and hydroxyl radicals ($\bullet OH$) that possess a strong oxidative ability towards organic compounds [32–33]. To clarify the role of the negative radicals in the photocatalytic reaction, separate quenching experiments were performed (as demonstrated in Fig. 5a). The addition of the superoxide radical scavenger (ascorbic acid (AA)) does influence the photodegradation. The hydroxyl radical quencher (*tert*-butyl alcohol (TBA)) plays a relatively weak role during the whole reaction process. After the injection of electrons to UBOC, the RhB molecules are activated to be positive charged RhB* with strong oxidation property. Meanwhile, the holes in the valence band of UBOC are transfer to the surface to contact with adsorbed RhB molecules, further oxidize the RhB to the corresponding cationic radicals. To clarify the role of the holes in the photocatalytic reaction, trietholamine (TEOA) was added to capture the hole before the reaction. As shown in Fig. 5a, the presence of TEOA almost terminates the photodegradation reaction. On the basis of the above results, it is clear that the superoxide radicals and holes do play important role in the photocatalytic process.

Based on the above discussions, a tentative photocatalytic degradation mechanism for RhB over UBOC can be proposed (as illustrated in Fig. 5b). Under solar light irradiation, photoinduced electron–hole pairs are generated from UBOC. With the help of self-induced internal electric filed and shortened transport route of ultrathin nanosheet, the photogenerated electrons and holes could

be separated and transferred to the surface of UBOC efficiently. The injection electrons from RhB and the photogenerated electrons from conduction band of UBOC can react with the surface-adsorbed O_2 molecules through only one-electron transfer to give activated superoxide radicals. Meanwhile, the RhB molecules are activated to be the corresponding cationic radicals by the holes leaving in RhB and the holes on the surface of UBOC. Finally, the RhB cationic radicals react with superoxide radicals, trending to be degraded. The detailed reactions are described by the following equations:

$$UBOC + hv \rightarrow h^+ + e^-$$

$$RhB + hv \rightarrow RhB* + e^-$$

$$h^+ + RhB \rightarrow RhB*$$

$$e^- + O_2 \rightarrow \bullet O_2^-$$

$$RhB* + \bullet O_2^- \rightarrow degraded products$$

4. Conclusions

Summarily, characteristic BiOCl 3D hierarchical architectures containing velvet-flowers that are assembled by ultrathin BiOCl nanosheets are facilely achieved via a hydrothermal process. The UBOC exhibits an impressive photodegradation efficiency and photocurrent response. After only 10 min under solar light irradiation, 99% photodegradation and 74% mineralization of RhB are realized. Meanwhile, the prepared UBOC exhibits an excellent anti-restack property. It is easy to be collected and recycled without any agglomeration problems. The suitable polarized internal electric field, the shortened charge-carries diffusion length and the enhanced light harvesting result in a high photodegradation rate and an outstanding photocurrent responses for UBOC, qualifying the UBOC as an excellent photocatalyst. This work develops a new tactic for high-performance photocatalyst design by means of ultrathin nanosheets.

Appendix A. Supplementary data

Supplementary data associated with this article can be found, in the online version, at http://dx.doi.org/10.1016/j.apcatb.2015.04.013.

References

[1] F.E. Osterloh, Chem. Soc. Rev. 42 (2013) 2294–2320.
[2] M. Wang, J. Ioccozia, L. Sun, C. Lin, Z. Lin, Energy Environ. Sci. 7 (2014) 2182–2202.
[3] T.R. Gordon, M. Cargnello, T. Paik, F. Mangolini, R.T. Weber, P. Fornasiero, C.B. Murray, J. Am. Chem. Soc. 134 (2012) 6751–6761.
[4] M. Zhang, J. Xu, R. Zong, Y. Zhu, Appl. Catal. B Environ. 147 (2014) 229–235.
[5] A. Liu, J. He, T. Yao, Z. Sun, W. Cheng, S. He, Y. Xie, Y. Peng, H. Cheng, Y. Sun, Y. Jiang, F. Hu, Z. Xie, W. Yan, Z. Pan, Z. Wu, S. Wei, Nat. Commun. 5 (2014) 5122.
[6] S. Semlali, T. Pigot, D. Flahaut, J. Allouche, S. Lacombe, L. Nicole, Appl. Catal. B Environ. 150–151 (2014) 656–662.
[7] Z. Xiong, X.S. Zhao, J. Am. Chem. Soc. 134 (2012) 5754–5757.
[8] F. Lei, Y. Sun, K. Liu, S. Gao, L. Liang, B. Pan, Y. Xie, J. Am. Chem. Soc. 136 (2014) 6826–6829.
[9] M. Guan, C. Xiao, J. Zhang, S. Fan, R. An, Q. Cheng, J. Xie, M. Zhou, B. Ye, Y. Xie, J. Am. Chem. Soc. 135 (2013) 10411–10417.
[10] S. Ida, Y. Okamoto, M. Matsuka, H. Hagiwara, T. Ishihara, J. Am. Chem. Soc. 134 (2012) 15773–15782.
[11] Y. Sun, Z. Sun, S. Gao, H. Cheng, Q. Liu, F. Lei, S. Wei, Y. Xie, Adv. Energy Mater. 4 (2014) 1300611.
[12] L. Liang, Y. Sun, F. Lei, S. Gao, Y. Xie, J. Mater. Chem. A. 2 (2014) 10647–10653.
[13] S. Sun, W. Wang, L. Zhang, E. Gao, D. Jiang, Y. Sun, Y. Xie, ChemSusChem 6 (2013) 1873–1877.
[14] K. Zhang, C. Liu, F. Huang, C. Zheng, W. Wang, Appl. Catal. B Environ. 68 (2006) 125–129.
[15] J. Jiang, K. Zhao, X. Xiao, L. Zhang, J. Am. Chem. Soc. 134 (2012) 4473–4476.
[16] J. Li, L. Zhang, Y. Li, Y. Yu, Nanoscale 6 (2014) 167–171.
[17] L. Zhang, W. Wang, S. Sun, D. Jiang, E. Gao, Appl. Catal. B Environ. 162 (2015) 470–474.
[18] K. Zhao, L. Zhang, J. Wang, Q. Li, W. He, J.J. Yin, J. Am. Chem. Soc. 135 (2013) 15750–15753.
[19] Y. Wu, B. Yuan, M. Li, W.H. Zhang, Y. Liu, C. Li, Chem. Sci. 6 (2015) 1873–1878.
[20] S. Wang, Z. Fang, Z. Wang, Z. Zheng, W. Feng, P. Liu, ACS Appl. Mater. Interfaces 6 (2014) 18423–18428.
[21] X. Zhang, Z. Ai, F. Jia, L. Zhang, J. Phys. Chem. C 112 (2008) 747–753.
[22] L.-P. Zhu, G.-H. Liao, N.-C. Bing, L.-L. Wang, Y. Yang, H.-Y. Xie, CrystEngComm. 12 (2010) 3791–3796.
[23] S. Peng, L. Li, P. Zhu, Y. Wu, M. Srinivasan, S.G. Mhaisalkar, S. Ramakrishna, Q. Yan, Chem-Asian J. 8 (2013) 258–268.
[24] K. Zhang, J. Liang, S. Wang, J. Liu, K. Ren, X. Zheng, H. Luo, Y. Peng, X. Zou, X. Bo, J. Li, X. Yu, Cryst. Growth Des. 12 (2012) 793–803.
[25] D.-H. Wang, G.-Q. Gao, Y.-W. Zhang, L.-S. Zhou, A.-W. Xu, W. Chen, Nanoscale 4 (2012) 7780–7785.
[26] J. Hu, W. Fan, W. Ye, C. Huang, X. Qiu, Appl. Catal. B Environ. 158–159 (2014) 182–189.
[27] X. Zhang, X. Liu, C. Fan, Y. Wang, Y. Wang, Z. Liang, Appl. Catal. B Environ. 132–133 (2013) 332–341.
[28] Y. Li, J. Liu, J. Jiang, J. Yu, Dalton Trans. 40 (2011) 6632–6634.
[29] T. Xiong, F. Dong, Z. Wu, RSC. Adv. 4 (2014) 56307–56312.
[30] F. Dong, Q. Li, Y. Zhou, Y. Sun, H. Zhang, Z. Wu, (2014) 9468–9480.
[31] X. Lin, T. Huang, F. Huang, W. Dong, J. Shi, J. Phys. Chem. B. 110 (2006) 24629–24634.
[32] M.A. Gondal, X. Chang, A.A. Al-Saadi, Z.H. Yamani, J. Zhang, G. Ji, J. Environ. Sci. Heal. Part A 47 (2012) 1192–1200.
[33] D. Wang, T. Kako, J. Ye, J. Am. Chem. Soc. 130 (2008) 2724–2725.

Yan Mi[a]
Liaoyong Wen[a]
Zhijie Wang[a]
Dawei Cao[a]
Yaoguo Fang[a]
Yong Lei[a,b,*]

[a] *Institute of Physics & Institute of Micro- and Nanotechnologies (IMN MacroNano®), Technische Universität Ilmenau 98693 Ilmenau, Germany*
[b] *Institute of Nanochemistry and Nanobiology, School of Enviromental and Chemical Engineering, Shanghai University, Shanghai 20044, PR China*

[*] Corresponding author. Tel.: +49 3677 693748; fax: +49 3677 693746.
E-mail address: yong.lei@tu-ilmenau.de (Y. Lei)

28 January 2015

3 April 2015

6 April 2015

Available online 8 April 2015